Direct Attenuation Correction Using Deep Learning for Cardiac SPECT: A Feasibility Study

Jaewon Yang[1], Luyao Shi[2], Rui Wang[3,4], Edward J. Miller[3,5], Albert J. Sinusas[2,3,5], Chi Liu[2,3], Grant T. Gullberg[1], and Youngho Seo[1]

[1]*Physics Research Laboratory, Department of Radiology and Biomedical Imaging, University of California San Francisco, San Francisco, California;* [2]*Biomedical Engineering, Yale University, New Haven, Connecticut;* [3]*Radiology and Biomedical Imaging, Yale University, New Haven, Connecticut;* [4]*Department of Engineering Physics, Tsinghua University, Beijing, China; and* [5]*Internal Medicine (Cardiology), Yale University, New Haven, Connecticut*

Dedicated cardiac SPECT scanners with cadmium-zinc-telluride cameras have shown capabilities for shortened scan times or reduced radiation doses, as well as improved image quality. Since most dedicated scanners do not have integrated CT, image quantification with attenuation correction (AC) is challenging and artifacts are routinely encountered in daily clinical practice. In this work, we demonstrated a direct AC technique using deep learning (DL) for myocardial perfusion imaging (MPI). **Methods:** In an institutional review board–approved retrospective study, 100 cardiac SPECT/CT datasets with ^{99m}Tc-tetrofosmin, obtained using a scanner specifically with a small field of view, were collected at the Yale New Haven Hospital. A convolutional neural network was used for generating DL-based attenuation-corrected SPECT ($SPECT_{DL}$) directly from noncorrected SPECT ($SPECT_{NC}$) without undergoing an additional image reconstruction step. The accuracy of $SPECT_{DL}$ was evaluated by voxelwise and segmentwise analyses against the reference, CT-based AC ($SPECT_{CTAC}$), using the 17-segment myocardial model of the American Heart Association. Polar maps of representative (best, median, and worst) cases were visually compared to illustrate potential benefits and pitfalls of the DL approach. **Results:** The voxelwise correlations with $SPECT_{CTAC}$ were 92.2% ± 3.7% (slope, 0.87; $R^2 = 0.81$) and 97.7% ± 1.8% (slope, 0.94; $R^2 = 0.91$) for $SPECT_{NC}$ and $SPECT_{DL}$, respectively. The segmental errors of $SPECT_{NC}$ scattered from −35% to 21% ($P < 0.001$), whereas the errors of $SPECT_{DL}$ stayed mostly within ±10% ($P < 0.001$). The average segmental errors (mean ± SD) were −6.11% ± 8.06% and 0.49% ± 4.35% for $SPECT_{NC}$ and $SPECT_{DL}$, respectively. The average absolute segmental errors were 7.96% ± 6.23% and 3.31% ± 2.87% for $SPECT_{NC}$ and $SPECT_{DL}$, respectively. Review of polar maps revealed successful reduction of attenuation artifacts; however, the performance of $SPECT_{DL}$ was not consistent for all subjects, likely because of different amounts of attenuation and different uptake patterns. **Conclusion:** We demonstrated the feasibility of direct AC using DL for SPECT MPI. Overall, our DL approach reduced attenuation artifacts substantially compared with $SPECT_{NC}$, justifying further studies to establish safety and consistency for clinical applications in stand-alone SPECT systems suffering from attenuation artifacts.

Key Words: cardiac SPECT; MPI; attenuation correction; deep learning

J Nucl Med 2021; 62:1645–1652
DOI: 10.2967/jnumed.120.256396

Received Sep. 4, 2020; revision accepted Feb. 16, 2021.
For correspondence or reprints, contact Jaewon Yang (jaewon.yang@ucsf.edu).
Published online February 26, 2021.
COPYRIGHT © 2021 by the Society of Nuclear Medicine and Molecular Imaging.

SPECT myocardial perfusion imaging (MPI) is the most widely applied noninvasive method for the detection and risk stratification of coronary artery disease (*1*). It is less costly and more widely available than PET MPI. However, since conventional SPECT systems are not optimized for cardiac imaging, dedicated cardiac SPECT scanners with cadmium-zinc-telluride (CZT) cameras have been developed constraining the entire detector area to imaging just the heart (*2*). The CZT cameras can achieve 5–10 times higher count sensitivity and 3–6 times faster scanning times than conventional sodium iodide SPECT cameras (*3*), resulting in higher image quality with lower radiation dose and promoting easier scheduling and greater patient satisfaction (*2*).

However, in daily clinical practice, artifacts are commonly observed for dedicated cardiac SPECT cameras, as they are for conventional SPECT cameras (*4*). Soft-tissue attenuation is the most common cause of artifacts and is usually due to the diaphragm, breast tissue, or obesity (*5*). Therefore, incorporation of attenuation correction (AC) into routine clinical practice is encouraged in order to reduce the artifacts and thus improve diagnostic accuracy (*6*). Nevertheless, AC is not performed as routine clinical practice for most dedicated cardiac SPECT systems not integrated with CT (*7*).

AC techniques for SPECT are categorized into 3 approaches to generating attenuation maps. The first approach is to perform transmission CT scans for generating AC maps—a capability that is available in integrated SPECT/CT systems but not in stand-alone SPECT systems, occupying approximately 80% of the market share (*8*). The second approach is to use line sources (most commonly ^{153}Gd), which may cause low-count AC maps and truncation artifacts (due to obesity) or cross-talk with emission data (*9*). The third approach is to estimate AC maps from emission data—an approach that is also classified as segmentation-based (*10*) or model-based (*11*) but is not practical because of time-consuming processes or computations.

Recently, it was demonstrated that attenuation maps could be directly estimated from the emission data using a deep learning (DL) model (*12*). In general, DL applications for AC have been actively investigated in PET/MRI to convert MR images directly to pseudo-CT images (*13*,*14*). Furthermore, a direct DL approach was proposed to convert noncorrected PET to corrected PET in image space without any additional reconstruction steps (*15*,*16*)—an approach that has not been applied to SPECT yet. Also, an indirect approach was demonstrated for stand-alone conventional SPECT scanners (*12*), requiring the reconstruction of full–field-of-

view (FOV) emission images for generating full-FOV attenuation maps. For this reason, such indirect approaches to generating attenuation maps as an intermediate step cannot be directly applied to dedicated cardiac SPECT scanners such as the Discovery NM 530c (GE Healthcare), whose geometry is unique, with a small FOV of about 19 cm in diameter (*17*). Therefore, a direct-conversion approach such as we present here is needed specifically for a scanner with a small FOV. It is worth noting that our DL approach cannot be directly compared with any indirect DL approach, such as that of Shi et al. (*12*).

Therefore, in this article we demonstrate a direct DL technique for CT-less AC in dedicated cardiac SPECT systems. Considering AC as a computer vision task, we hypothesized that DL can recognize clinically relevant uptake patterns in both noncorrected ($SPECT_{NC}$) and DL-corrected ($SPECT_{DL}$) images for removing attenuation-involved artifacts in SPECT MPI.

MATERIALS AND METHODS

SPECT Datasets

The institutional review board approved this retrospective study, and the requirement to obtain informed consent was waived. One hundred datasets (58 male and 42 female) were collected from cardiac stress-only ^{99m}Tc-tetrofosmin SPECT using a Discovery NM/CT 570c scanner (GE Healthcare) at Yale New Haven Hospital. The characteristics of subjects are not available because of the deidentification performed for the data transfer to the University of California San Francisco. CT images (120 kVp, 50 mA, and rotation time of 0.4 s) were aligned with $SPECT_{NC}$ images in the myocardium region through the AC quality control package routinely used in clinical practice. Using the iterative Green's one-step-late algorithm (*18*) image reconstructions (70 × 70 × 50 matrix size with 4-mm voxel size) were performed with 30 iterations and postfiltering (10th-order Butterworth filter, 0.4 cm^{-1} cutoff) for $SPECT_{NC}$ and with 60 iterations and postfiltering (seventh-order Butterworth filter, 0.37 cm^{-1} cutoff) for SPECT with CT-based AC ($SPECT_{CTAC}$). All the reconstruction and filter parameters are clinically used, but no established scatter correction is routinely applied for Discovery NM/CT 570c scanners with CZT detectors at Yale New Haven Hospital.

Deep Convolutional Neural Network (DCNN)

The proposed DL model aims to transform $SPECT_{NC}$ to $SPECT_{CTAC}$ directly in image space ($SPECT_{DL}$), without generating μ-maps for conventional image reconstruction combined with AC (Fig. 1). The proposed DCNN is an extended 3-dimensional version of our previous work (*15*). Different from conventional scanners, dedicated cardiac SPECT scanners allow a limited FOV to include at least the whole heart, which enables ideal 3-dimensional model training without separating the left ventricle into smaller patches. The original patch size of 70 × 70 × 50 was reduced to 64 × 64 × 32 by removing the edges of each patch for enabling downsampling (64 → 32 → … → 4) in each dimension. Our DCNN consists of 5 encoder–decoder stages symmetrically concatenated with skip connections. In each stage, convolution with 3 × 3 × 3 kernels, batch normalization, and a rectified linear unit is sequentially performed twice. Between stages, the downsampling and upsampling are done by 2 × 2 × 2 maximum pooling and bilinear interpolation, respectively. The original design proposed in our previous work (*15*) was modified to a 3-dimensional network architecture for this study.

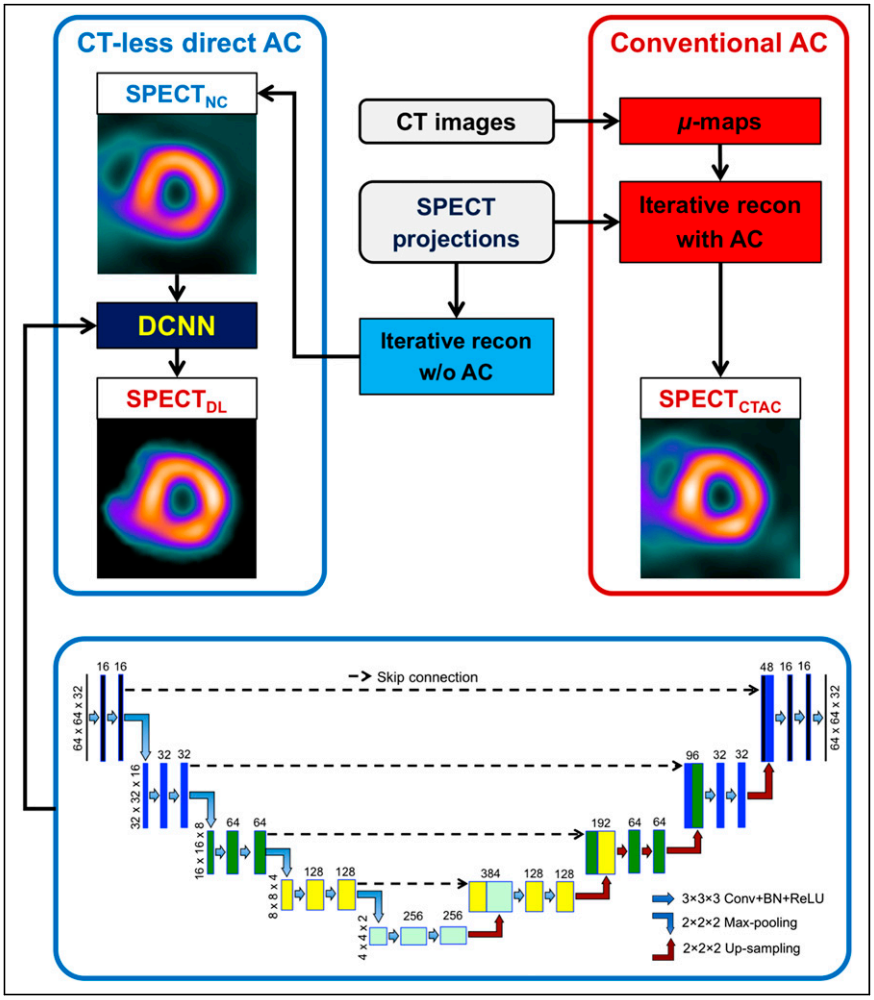

FIGURE 1. Schematic of proposed DCNN-based AC performed in image space (left), compared with conventional AC performed through system matrix during SPECT image reconstruction (right). BN = batch normalization; conv = convolution; recon = reconstruction; ReLU = rectified linear unit.

DCNN Training and Testing

The DCNN was trained and tested with paired input ($SPECT_{NC}$) and output ($SPECT_{CTAC}$) patches using 10-fold cross validation without external validation: that is, the model was trained with 9 groups (10 patches in each group) and tested with the tenth one, and this process was repeated 10 times. The raw values (absolute counts) of each patch were normalized by its maximum to reduce the dynamic range of input/output values. In the patches, low counts in the myocardium were considered background noise and removed by binary masking (*15*). Before being fed into the model, 90 input patches were randomly shuffled, rotated (≤15° in transaxial view), and translated horizontally (≤10 pixels), vertically (≤10 pixels), and axially (≤3 pixels) for data augmentation. A learning rate initialized by

0.001 was reduced to three fourths of its current value in the course of training if the loss did not decrease in 25 epochs. Weights for convolution were initialized with the He-initializer (*19*), and all biases were initialized with zero. Mean squared error (or L2 loss) and RMSprop optimizer (*20*) were used for optimizing weights and biases. The loss was converged in 1,500 epochs, and the training was stopped at that point, which was empirically determined through loss curves and consistent across all the folds. The hyperparameters empirically chosen in our previous work (*15*) were adapted for this study through hyperparameter tuning.

The proposed model was implemented using TensorFlow (version 1.12.0) and Keras libraries (version 2.2.4). Model training and testing were performed on an Ubuntu server with a single Tesla V100 (NVIDIA) graphics processing unit. The training took approximately 100 min to reach stability. After training the model, it takes only 0.5 s on average to generate $SPECT_{DL}$ volumetric images (64 × 64 × 32).

Quantitative Analysis

The overall quantitative accuracy of $SPECT_{DL}$ was evaluated and compared with the reference, $SPECT_{CTAC}$. For voxelwise analysis, the normalized root mean square error, peak signal-to-noise ratio, and structural similarity index were quantified. For segmentwise analysis, polar maps were generated and compared using the 17-segment myocardial model of the American Heart Association for the left ventricle, which was adopted from Herzog et al. (*21*). A measured count of each segment was normalized by the maximum count of 17 segments. The relative percentage count of each segment was computed, and an error (i.e., $SPECT_{DL} - SPECT_{CTAC}$) was assessed. Additionally, the effects of sex (58 men vs. 42 women) and hepatic uptake (44 subjects with high liver uptake [HLU] vs. 56 with low liver uptake [LLU]) were investigated through the segmentwise analysis separately for each cohort. Although information on patient weight and height was not available for computing body mass index, the volume of each patient was estimated from CT-derived attenuation maps to investigate any correlation between chest volumes and average segmental errors across subjects.

Illustration of Representative Cases

Three categories of subjects were selected to illustrate the overall qualitative assessment of $SPECT_{DL}$. First, 3 subjects with the smallest mean segmental error were selected as examples of $SPECT_{DL}$ that achieved quantitatively the most accurate correction. Second, 3 subjects with the 25th, 50th, and 75th percentiles of absolute mean segmental error were chosen as examples of $SPECT_{DL}$ that achieved quantitatively median accuracy. Finally, 2 subjects with the highest and lowest mean segmental errors were selected to display examples that our DL model was not able to correct accurately.

Statistics

A joint histogram was used to show the distribution of voxelwise correlation of $SPECT_{DL}$ with the reference. Also, the error distributions of all segments of all 100 subjects (17 × 100 = 1,700 segments in total) for $SPECT_{DL}$ were displayed in Bland–Altman and box plots. A paired *t* test was performed to compare the segmental uptake values of $SPECT_{DL}$ with those of the reference. A *P* value of less than 0.05 was considered to indicate statistical significance.

Polar maps were generated using the Cardiac PET Modeling Tool (version 3.8; PMOD Technologies). All processing and analyses were performed in MATLAB (version R2015b; The MathWorks).

RESULTS

For voxelwise analysis, the normalized root mean square errors were 0.232 ± 0.077 and 0.148 ± 0.095 for $SPECT_{NC}$ and $SPECT_{DL}$, respectively; the respective peak signal-to-noise ratios were 31.3 ± 2.8 and 36.2 ± 4.1; and the respective structural similarity indices were 0.984 ± 0.008 and 0.993 ± 0.006. Consistently, the voxelwise correlations were 92.2% ± 3.7% (slope, 0.87; R^2 = 0.81) and 97.7% ± 1.8% (slope, 0.94; R^2 = 0.91) for $SPECT_{NC}$ and $SPECT_{DL}$, respectively (Fig. 2).

For segmentwise analysis, the errors of $SPECT_{NC}$ scattered from −35% to 21%, whereas those of $SPECT_{DL}$ stayed mostly within ±10% (Fig. 3). Consequently, the average errors (mean ± SD) were −6.11% ± 8.06% and 0.49% ± 4.35% for $SPECT_{NC}$ and $SPECT_{DL}$, respectively, and the respective average absolute errors were 7.96% ± 6.23% and 3.31% ± 2.87%, which were consistent with the sex-dependent and hepatic uptake–dependent results where the average errors of $SPECT_{NC}$ were substantially reduced through DL (Table 1). All results were statistically

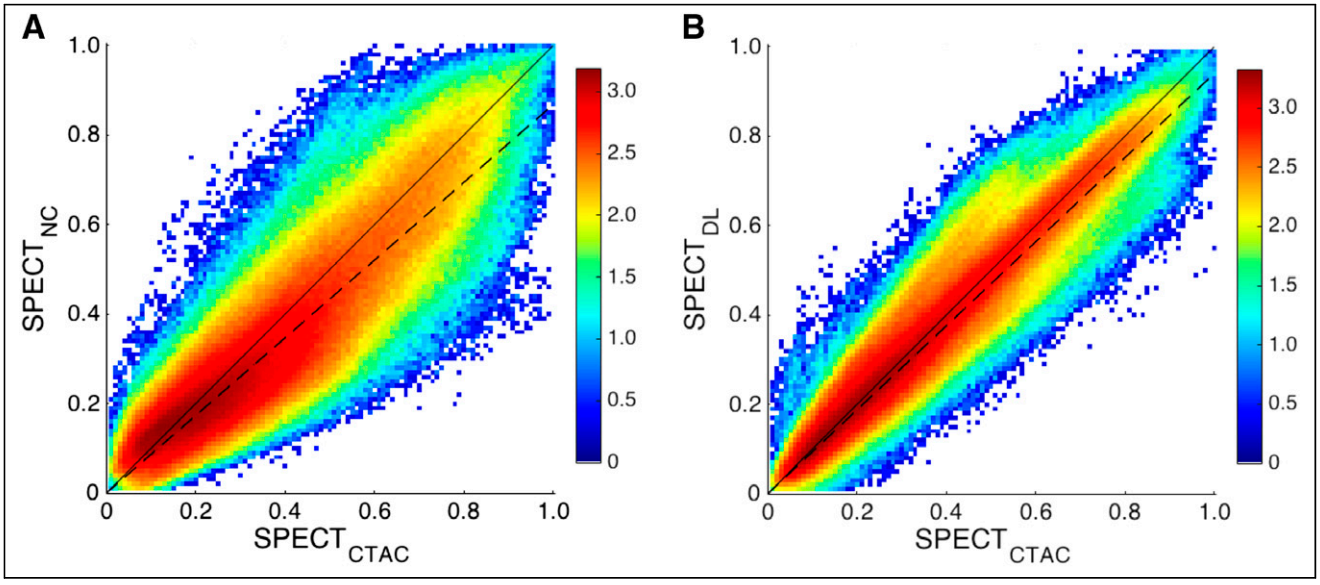

FIGURE 2. Joint histogram of voxels in the myocardium: $SPECT_{NC}$ vs. $SPECT_{CTAC}$ (A) and $SPECT_{DL}$ vs. $SPECT_{CTAC}$ (B). Counts were log-scaled (i.e., $\log_{10}$(counts)) to visualize small counts in joint histograms.

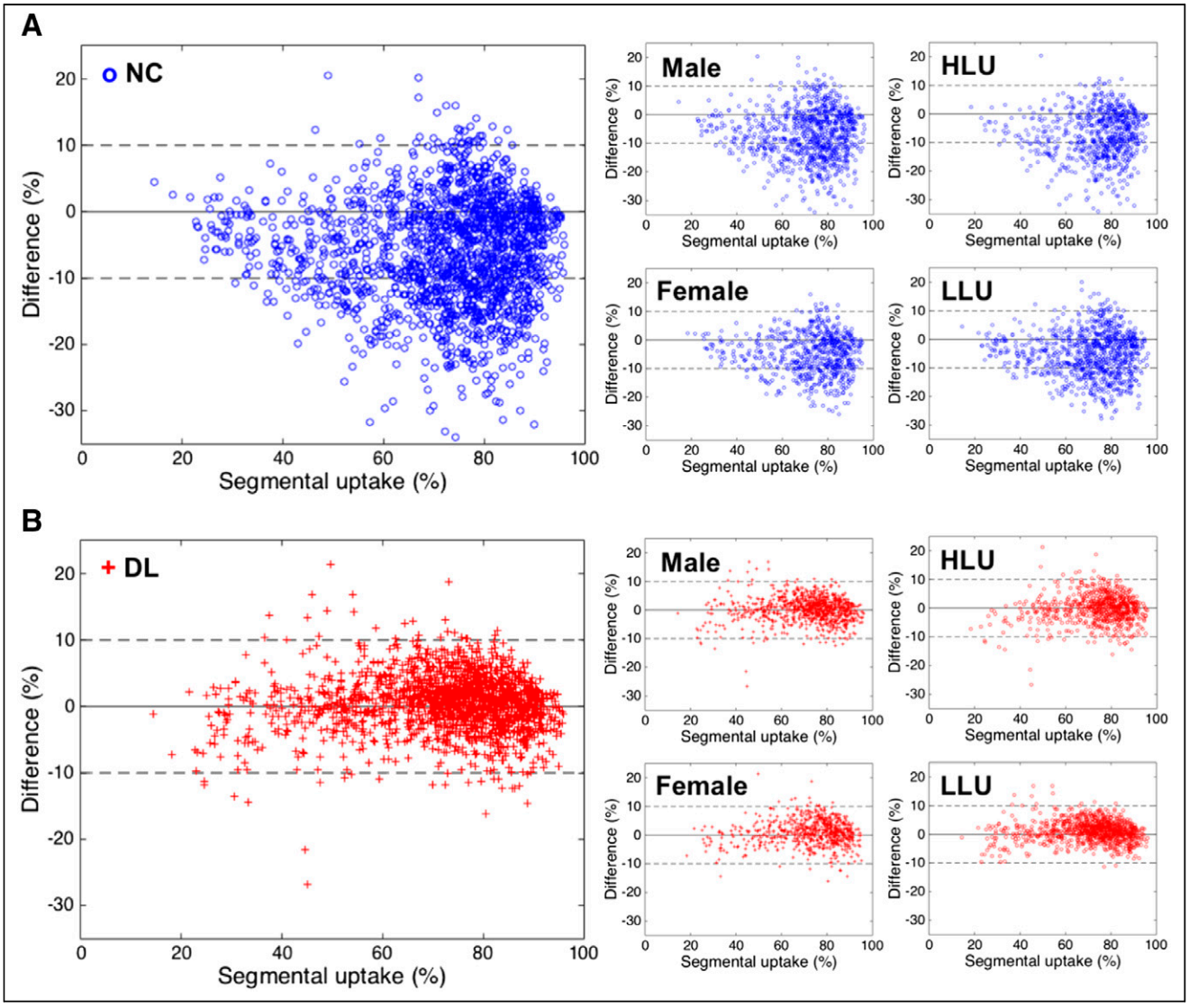

FIGURE 3. Bland–Altman plots for percentage segmental errors across all subjects, male and female subjects, and subjects with HLU and LLU: $SPECT_{NC}$ (A) and $SPECT_{DL}$ (B).

significant, except for the male sex ($P = 0.10$) and subjects with HLU ($P = 0.25$).

Figure 4 shows that DL reduced the error distributions of all segments close to a mean of zero within ±10% variation across all subjects, as was consistent with the corresponding error distributions for the male sex, the female sex, and subjects with HLU and LLU (Supplemental Fig. 1; supplemental materials are available at http://jnm.snmjournals.org). Specifically, DL reduced the average absolute error of $SPECT_{NC}$ by more than 70% for segments 4, 9, 10, and 15; more than 60% for segments 3, 5, and 11; more than 50% for segments 8 and 14; more than 40% for segments 16 and 17; and more than 17% for the rest. The box plot of each subject across all 17 segments is shown in Supplemental Figure 2. In analyzing the correlation between patients' chest volumes and average segmental errors, no correlation was found for either $SPECT_{NC}$ ($\rho = 0.016$) or $SPECT_{DL}$ ($\rho = 0.021$), though a moderate nonlinear (affine) correlation ($\rho = 0.6264$) was found between $SPECT_{NC}$ and $SPECT_{DL}$ (Supplemental Fig. 3).

Three categories of subjects are described in Table 2 to illustrate the overall performance of our DL approach. Figure 5 illustrates accurately corrected attenuation artifacts in the right coronary artery (RCA) territory of $SPECT_{DL}$. In Figure 6, artifacts were accurately corrected in the first 2 cases (25th and 50th percentiles) in the RCA of $SPECT_{DL}$, though no remarkable visual difference between $SPECT_{NC}$ and $SPECT_{CTAC}$ was observed for the last case (75th percentile). Figure 7 illustrates 2 cases with substantially overestimated $SPECT_{DL}$ in the RCA and left circumflex (LCx) artery and substantially underestimated $SPECT_{DL}$ in the RCA and left anterior descending (LAD) artery.

DISCUSSION

We demonstrated that our DL model substantially reduced the attenuation artifacts of $SPECT_{NC}$, illustrating its potential benefits and pitfalls. To our knowledge, this is the first work to demonstrate a CT-less direct AC in image space, as an accelerated one-step process for SPECT MPI in a dedicated SPECT system.

TABLE 1
Average Error, Average Absolute Error, and Correlation Coefficients of All Segments Across All Subjects

Cohort	SPECT type	Error (%)	|Error| (%)	Pearson's correlation coefficient (%)	*P*
All (n = 100)	NC	−6.11 ± 8.06	7.96 ± 6.23	88.05	<0.001
	DL	0.49 ± 4.35	3.31 ± 2.87	96.17	<0.001
Male (n = 58)	NC	−6.96 ± 8.62	8.80 ± 6.72	86.66	<0.001
	DL	0.22 ± 4.28	3.19 ± 2.85	96.22	0.10
Female (n = 42)	NC	−4.95 ± 7.05	6.80 ± 5.29	90.36	<0.001
	DL	0.85 ± 4.44	3.46 ± 2.90	96.12	<0.001
HLU (n = 44)	NC	−7.30 ± 8.28	8.71 ± 6.79	86.72	<0.001
	DL	−0.21 ± 4.99	3.75 ± 3.30	94.75	0.25
LLU (n = 56)	NC	−5.18 ± 7.75	7.38 ± 5.70	89.36	<0.001
	DL	1.03 ± 3.69	2.96 ± 2.43	97.33	<0.001

Data are mean ± SD.

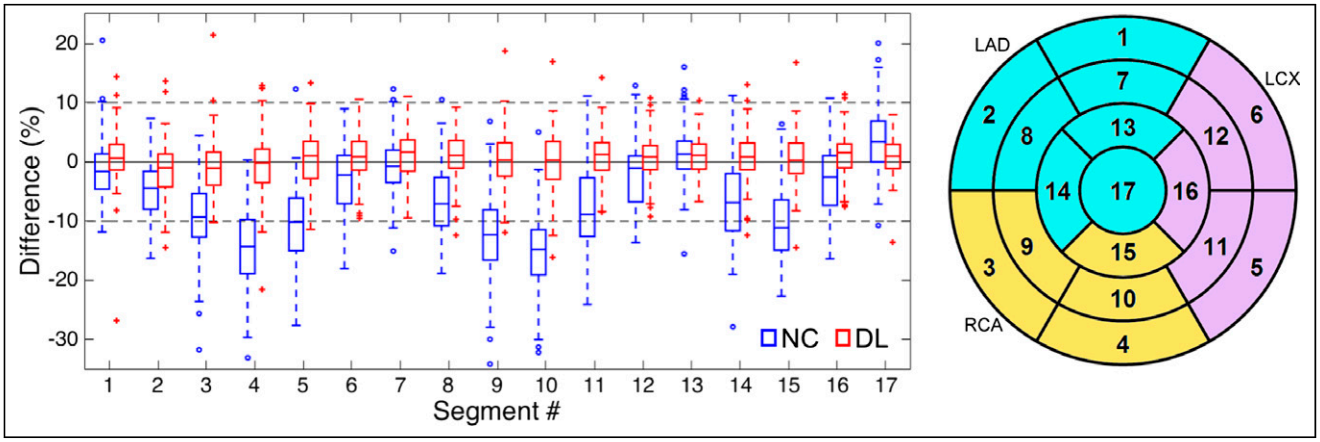

FIGURE 4. Polar map (right) and box plots (left) for percentage segmental errors across all subjects.

TABLE 2
Selected Subjects for Figures 5–7 and Their Average Errors Across 17 Segments for $SPECT_{DL}$ and $SPECT_{NC}$

Subject no.	Figure no.	DL error (%)	NC error (%)	Criteria for DL selection
66 (male, HLU)	5A	0.10 ± 4.08	−12.61 ± 10.04	Smallest |error|
54 (male, HLU)	5B	0.10 ± 2.26	−8.73 ± 8.44	Smallest |error|
93 (male, LLU)	5C	−0.10 ± 2.99	−6.32 ± 6.69	Smallest |error|
9 (male, LLU)	6A	1.10 ± 2.46	−9.04 ± 7.49	25th percentile |error|
89 (male, HLL)	6B	1.99 ± 3.05	−4.59 ± 6.85	50th percentile |error|
77 (female, HLL)	6C	3.15 ± 4.07	1.17 ± 5.25	75th percentile |error|
7 (male, LLU)	7A	9.20 ± 4.55	2.65 ± 2.63	Most overestimated error
57 (female, HLU)	7B	−7.21 ± 4.85	−12.25 ± 7.25	Most underestimated error

Supplemental Figure 1 provides average segmental errors of all subjects through box plots.

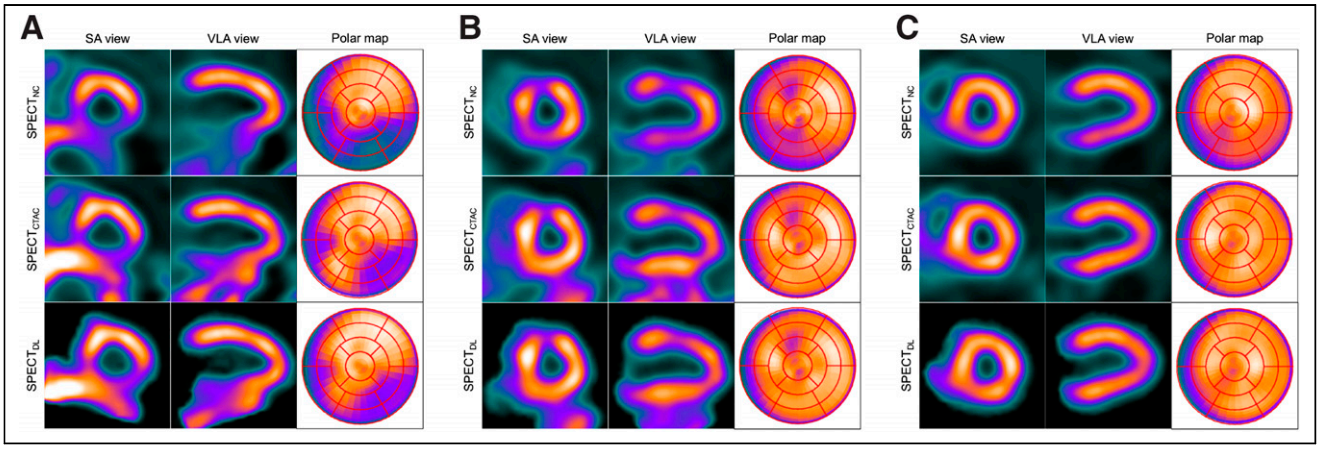

FIGURE 5. Examples of 3 subjects (A, male; B, male; C, male) with smallest absolute mean segmental error in short-axis (SA) and vertical long-axis (VLA) views and polar maps.

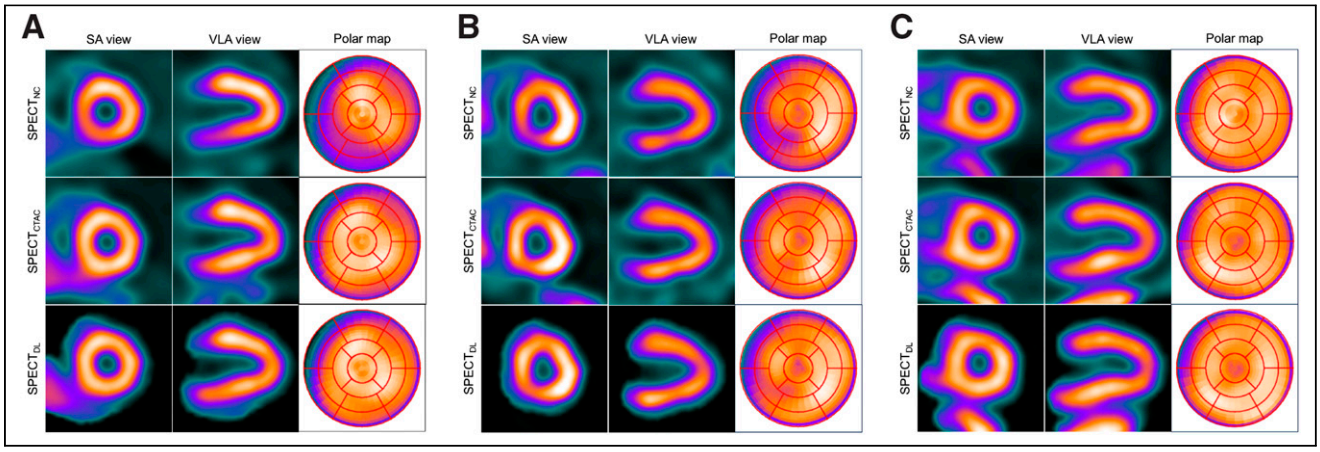

FIGURE 6. Examples of 3 subjects with 25th (A, male), 50th (B, male), and 75th (C, female) percentiles of absolute mean segmental errors in short-axis (SA) and vertical long-axis (VLA) views and polar maps.

There are several technical and clinical benefits to our DL approach for SPECT MPI. From a technical perspective, the biggest potential advantage is in removing the need to generate an attenuation map, which is an essential step in conventional image reconstruction. Most dedicated cardiac SPECT systems (*7*) and approximately 80% of SPECT systems in the market are stand-alone (i.e., not combined with CT) (*8*), which acknowledges the potential value of our DL approach. Also, our direct DL approach is much simpler and faster (<1 s) than conventional approaches that require an additional reconstruction step with time-consuming computation. From a clinical perspective, when approaches such as conventional AC methods or alternative prone imaging are not possible (*5*), our DL model could potentially incorporate AC into routine clinical practice (*6*) and efficiently improve the accuracy of diagnosis in existing stand-alone SPECT systems, since attenuation artifacts due to soft tissue are more likely to be misinterpreted as fixed defects in healthy patients with normal heart function (*22*). Also, our model trained with datasets acquired in a conventional SPECT/CT scanner could be applied to different datasets acquired in a stand-alone scanner if images are reconstructed with similar parameters and their pixel sizes are consistent across different scanners. For example, it would be feasible to apply our DL model trained with datasets from a Discovery NM/CT 570c (combined SPECT/CT) to new datasets acquired in a Discovery NM 530c (stand-alone) since the geometries and hardware components of both scanners are very close and thus their $SPECT_{NC}$ image qualities are similar. Nevertheless, it is expected that an indirect DL approach such as generating pseudo-CT scans (*12*) would perform more consistently than our direct DL approach, since the indirect approach keeps every aspect of the conventional image reconstruction; however, a direct approach such as ours needs to learn attenuation physics and statistics by a DCNN, which requires large amounts of normative training data. Another important clinical merit of our CT-less DL approach is reduction of the radiation dose from CT, potentially leading to a substantial decrease in lifetime cancer risk (*9*), specifically for pediatric patients who are much more sensitive to radiation (*10,11*).

The general rules of attenuation in SPECT MPI were derived from the literature as follows (*5*): first, in men more often than in women, the left hemidiaphragm results in potential perfusion artifacts in the RCA, and these are more accentuated with abdominal protuberance, an elevated left hemidiaphragm, or obesity; second, in women more often than in men, breast attenuation causes potential perfusion artifacts in the LAD artery or LCx artery; and third, the high-uptake liver may create artifacts in the inferior wall. Our result was consistent with these general rules in many respects.

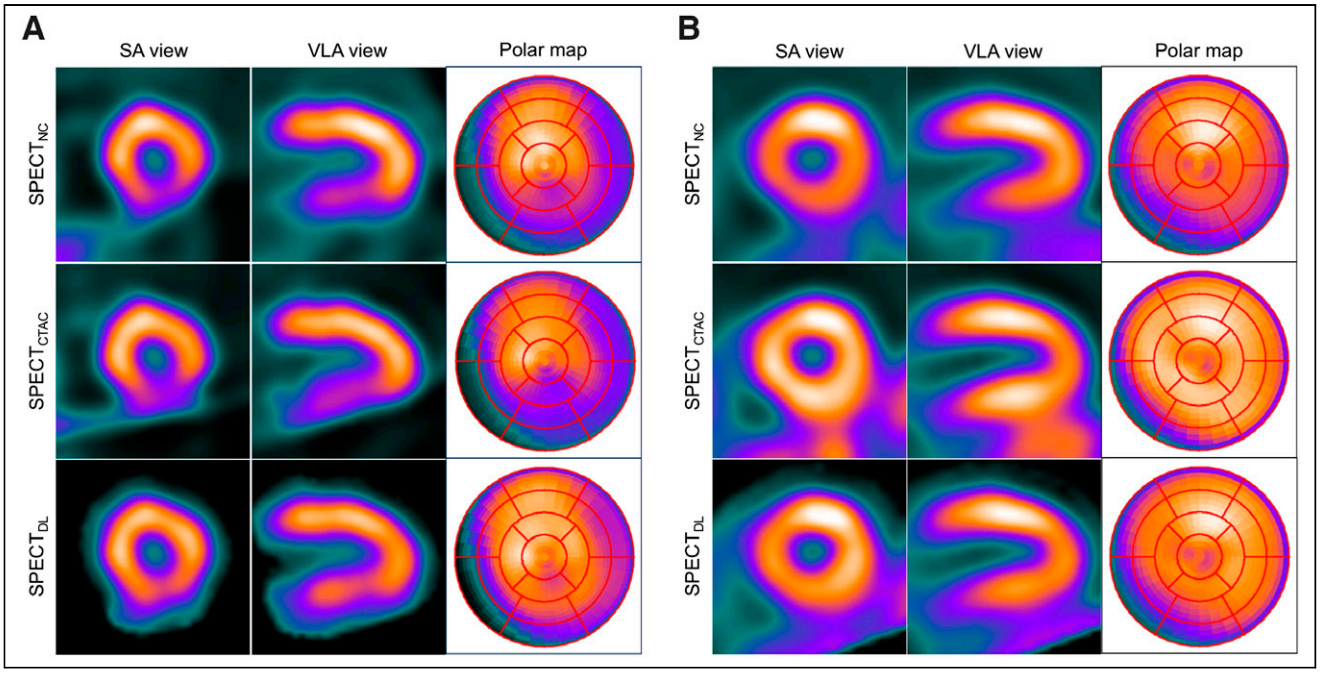

FIGURE 7. Examples of 2 subjects with most overestimated (A, male) and most underestimated (B, female) mean segmental errors in short-axis (SA) and vertical long-axis (VLA) views and polar maps.

Overall, Figure 4 confirmed the most important rule—the first one—in that large errors were found mostly in the RCA of $SPECT_{NC}$ but were corrected in $SPECT_{DL}$. Our DL approach substantially reduced artifacts across all RCA, LAD artery, and LCx artery territories. The errors of $SPECT_{NC}$ in the LAD and LCx arteries were relatively much smaller than those in the RCA for both men and women (Supplemental Fig. 1A), implying that breast attenuation (the second rule) was not dominant in our datasets. The slightly higher error of $SPECT_{NC}$ regarding the male sex might be because men are generally taller and heavier than women (*23*) but could not be thoroughly explained because we lacked information on subject height and weight. The larger average error of $SPECT_{NC}$ regarding subjects with HLU (Supplemental Fig. 1B) was consistent with the third rule.

There is always a risk that any new DL models may miss important patterns or generate pseudo patterns when exposed to new test data with different characteristics (*24*). Thus, representative cases were selected according to subject-specific quantitative results, as was appropriate and desirable for illustrating specific (best, median, and worst) cases. The visual performance of our DL approach was not consistent across all subjects, likely because of different amounts of soft tissue and different uptake patterns, as was inferred from the literature demonstrating substantially degraded image quality of $SPECT_{NC}$ for obese patients (*5*). However, at least in our dataset, there was no correlation between patients' chest volumes and average errors for either $SPECT_{NC}$ or $SPECT_{DL}$ (Supplemental Fig. 3). From the perspective of model training, since our DL model was optimized in only our limited dataset, the current model might not be able to achieve high accuracy for such cases (Fig. 7), whose attenuation artifacts might be unique and very different from the artifacts of other subjects. Therefore, there is still room to improve the accuracy of our model toward clinical translation.

Despite the promising results, our study had several limitations. First, 100 subjects may not be enough to represent all possible patterns involving attenuation artifacts. For example, the female population might not contain significant breast attenuation, implying the need to construct a large dataset with more diverse cases for future studies. Second, the clinical information (weight, height, clinical interpretation) was missing because of the deidentification, and a thorough investigation of the effects of such information on the current results was beyond the scope of this study. Third, no observer study or clinical interpretation (e.g., scoring $SPECT_{DL}$ vs. $SPECT_{CTAC}$) was performed, though summed perfusion scores derived from a reference dataset would improve the quality of this study; however, the uptake distribution of $SPECT_{CTAC}$ (i.e., the reference standard) was not uniform, as shown in the *x*-axis of the Bland–Altman plot (Fig. 3), and thus a reference dataset could not be derived for the scoring. Fourth, $SPECT_{CTAC}$ might include unexpected artifacts because of uncorrected scatter produced by subdiaphragmatic high-uptake organs (*25*). Unfortunately, conventional scatter correction approaches are not applicable to Discovery NM/CT 570c scanners because of the unique energy spectrum of pixelated CZT detectors, with a tailing effect caused by incomplete charger and interdetector scatters. Thus, clinical adoption of CZT-specific scatter correction methods is needed in the future (*26*,*27*). Finally, the right ventricle was unseen in $SPECT_{DL}$ because low-count voxels in the myocardium were considered background noise and removed by binary masking; however, an advanced network architecture might enable the binary masking to be skipped.

Therefore, for future work, it would be important to construct a large normative database with a greater number of diverse and outlier cases to investigate the effects of patient characteristics on model training and evaluation, deleting data with unexpected artifacts (e.g., attenuation artifacts due to a misalignment between SPECT and CT) based on physicians' interpretation. Also, it would be of great value to develop a validation program to evaluate large test datasets efficiently using automatic myocardium segmentation (*28*) and image quality assessment (*29*), which could

accelerate quantitative and qualitative analyses. These future efforts would establish the safety and consistency required for reliable interpretation toward clinical translation.

CONCLUSION

We demonstrated the feasibility of direct AC using DL for SPECT MPI, illustrating potential benefits and pitfalls. Overall, the DL model reduced attenuation artifacts substantially compared with $SPECT_{NC}$, justifying further studies to establish safety and consistency for clinical applications in stand-alone SPECT systems suffering from attenuation artifacts.

DISCLOSURE

This study was supported by the National Institutes of Health under grants R01HL135490, R01EB026331, and R01HL123949 and by American Heart Association award 18PRE33990138. No other potential conflict of interest relevant to this article was reported.

KEY POINTS

QUESTION: Is it feasible to use DL for CT-less AC in image space for MPI in a dedicated cardiac SPECT system?

PERTINENT FINDINGS: In a cohort study evaluating $SPECT_{DL}$ in 100 patients undergoing SPECT MPI with and without AC, our DL approach achieved quantitative and qualitative accuracy comparable to that of conventional $SPECT_{CTAC}$, reducing the attenuation artifacts observed in $SPECT_{NC}$.

IMPLICATIONS FOR PATIENT CARE: This DL technique demonstrated its potential to efficiently reduce the attenuation artifacts observed in stand-alone SPECT systems and thus improve the sensitivity and specificity of clinical interpretation.

REFERENCES

1. Hage FG, AlJaroudi WA. Review of cardiovascular imaging in the Journal of Nuclear Cardiology in 2017. Part 2 of 2: myocardial perfusion imaging. *J Nucl Cardiol*. 2018;25:1390–1399.
2. Garcia EV, Faber TL, Esteves FP. Cardiac dedicated ultrafast SPECT cameras: new designs and clinical implications. *J Nucl Med*. 2011;52:210–217.
3. Esteves FP, Raggi P, Folks RD, et al. Novel solid-state-detector dedicated cardiac camera for fast myocardial perfusion imaging: multicenter comparison with standard dual detector cameras. *J Nucl Cardiol*. 2009;16:927–934.
4. Kao YH, Better N. D-SPECT: new technology, old tricks. *J Nucl Cardiol*. 2016;23:311–312.
5. Singh B, Bateman TM, Case JA, Heller G. Attenuation artifact, attenuation correction, and the future of myocardial perfusion SPECT. *J Nucl Cardiol*. 2007;14:153–164.
6. Heller GV, Links J, Bateman TM, et al. American Society of Nuclear Cardiology and Society of Nuclear Medicine joint position statement: attenuation correction of myocardial perfusion SPECT scintigraphy. *J Nucl Cardiol*. 2004;11:229–230.
7. Allie R, Hutton BF, Prvulovich E, Bomanji J, Michopoulou S, Ben-Haim S. Pitfalls and artifacts using the D-SPECT dedicated cardiac camera. *J Nucl Cardiol*. 2016;23:301–310.
8. Global SPECT market 2017-2021. Technavio website. https://www.technavio.com/report/global-medical-imaging-global-spect-market-2017-2021. Published March 2017. Accessed May 20, 2021.
9. Pazhenkottil AP, Kaufmann PA, Gaemperli O. Attenuation correction in stress-only myocardial perfusion imaging. *J Nucl Cardiol*. 2017;24:402–404.
10. Núñez M, Prakash V, Vila R, Mut F, Alonso O, Hutton BF. Attenuation correction for lung SPECT: evidence of need and validation of an attenuation map derived from the emission data. *Eur J Nucl Med Mol Imaging*. 2009;36:1076–1089.
11. Cade SC, Arridge S, Evans MJ, Hutton BF. Use of measured scatter data for the attenuation correction of single photon emission tomography without transmission scanning. *Med Phys*. 2013;40:082506.
12. Shi L, Onofrey JA, Liu H, Liu YH, Liu C. Deep learning-based attenuation map generation for myocardial perfusion SPECT. *Eur J Nucl Med Mol Imaging*. 2020;47:2383–2395.
13. Leynes AP, Yang J, Wiesinger F, et al. Zero-echo-time and Dixon deep pseudo-CT (ZeDD CT): direct generation of pseudo-CT images for pelvic PET/MRI attenuation correction using deep convolutional neural networks with multiparametric MRI. *J Nucl Med*. 2018;59:852–858.
14. Gong K, Yang J, Kim K, El Fakhri G, Seo Y, Li Q. Attenuation correction for brain PET imaging using deep neural network based on Dixon and ZTE MR images. *Phys Med Biol*. 2018;63:125011.
15. Yang J, Park D, Gullberg GT, Seo Y. Joint correction of attenuation and scatter in image space using deep convolutional neural networks for dedicated brain ^{18}F-FDG PET. *Phys Med Biol*. 2019;64:075019.
16. Shiri I, Arabi H, Geramifar P, et al. Deep-JASC: joint attenuation and scatter correction in whole-body ^{18}F-FDG PET using a deep residual network. *Eur J Nucl Med Mol Imaging*. 2020;47:2533–2548.
17. Wu J, Liu C. Recent advances in cardiac SPECT instrumentation and imaging methods. *Phys Med Biol*. 2019;64:06TR01.
18. Green PJ. Bayesian reconstructions from emission tomography data using a modified EM algorithm. *IEEE Trans Med Imaging*. 1990;9:84–93.
19. He K, Zhang X, Ren S, Sun J. Delving deep into rectifiers: surpassing human-level performance on ImageNet classification. arXiv website. https://arxiv.org/abs/1502.01852. Published February 6, 2015. Accessed May 20, 2021.
20. Tieleman T, Hinton G. Lecture 6.5-rmsprop: Divide the gradient by a running average of its recent magnitude. COURSERA. 2012;4:26–31.
21. Herzog BA, Buechel RR, Husmann L, et al. Validation of CT attenuation correction for high-speed myocardial perfusion imaging using a novel cadmium-zinc-telluride detector technique. *J Nucl Med*. 2010;51:1539–1544.
22. DePuey EG, Rozanski A. Using gated technetium-99m-sestamibi SPECT to characterize fixed myocardial defects as infarct or artifact. *J Nucl Med*. 1995;36:952–955.
23. Ogden CL, Fryar CD, Carroll MD, Flegal KM. Mean body weight, height, and body mass index, United States 1960-2002. *Adv Data*. 2004;(347):1–17.
24. Zaharchuk G. Next generation research applications for hybrid PET/MR and PET/CT imaging using deep learning. *Eur J Nucl Med Mol Imaging*. 2019;46:2700–2707.
25. Dvorak RA, Brown RK, Corbett JR. Interpretation of SPECT/CT myocardial perfusion images: common artifacts and quality control techniques. *Radiographics*. 2011;31:2041–2057.
26. Pourmoghaddas A, Vanderwerf K, Ruddy TD, Glenn Wells R. Scatter correction improves concordance in SPECT MPI with a dedicated cardiac SPECT solid-state camera. *J Nucl Cardiol*. 2015;22:334–343.
27. Fan P, Hutton BF, Holstensson M, et al. Scatter and crosstalk corrections for ^{99m}Tc/^{123}I dual-radionuclide imaging using a CZT SPECT system with pinhole collimators. *Med Phys*. 2015;42:6895–6911.
28. Wang T, Lei Y, Tang H, et al. A learning-based automatic segmentation and quantification method on left ventricle in gated myocardial perfusion SPECT imaging: a feasibility study. *J Nucl Cardiol*. 2020;27:976–987.
29. Renieblas GP, Nogues AT, Gonzalez AM, Gomez-Leon N, Del Castillo EG. Structural similarity index family for image quality assessment in radiological images. *J Med Imaging (Bellingham)*. 2017;4:035501.